Quantifying thermal and nonthermal contributions to disorder in ultrashort laser irradiated germanium: Nonadiabatic quantum molecular dynamics study

Yungok Ihm [1,2,*] Je Young Ahn,[1] and Ji Hoon Shim[1,2,3,†]

[1]*Department of Chemistry, Pohang University of Science and Technology, Pohang 37673, Korea*
[2]*Photon Science Center, Pohang University of Science and Technology, Pohang 37673, Korea*
[3]*Division of Advanced Materials Science, Pohang University of Science and Technology, Pohang 37673, Korea*

(Received 18 September 2023; revised 3 April 2024; accepted 19 April 2024; published 9 May 2024)

We elucidate the origin of the ultrashort laser-driven lattice disorder in germanium through nonadiabatic quantum molecular dynamics simulations. The total disorder is dissected into disorder components arising from electron-phonon coupling, covalent bond softening, and ionic thermal activation caused by potential energy surface modification, using which thermal and nonthermal effects are quantified. We find that, although the bond softening effect initially dominates irrespective of the excitation density, the eventual ultrashort laser-driven phase transition involves both the thermal and nonthermal elements in it, with the level of their effects regulated by the electronic excitation density.

DOI: 10.1103/PhysRevB.109.174306

I. INTRODUCTION

Ultrashort laser-induced phase transitions have been of pivotal interest over the past decades [1–9]. A femtosecond laser drives the target system into highly nonequilibrium states of hot electrons and cold lattice due to the high energy deposition rate in the electrons. Empowered by the unprecedented single-bunch brightness of the x-ray probe from the free-electron laser, the interrogation of the structural dynamics of materials at the nanometer and picosecond spatiotemporal scales is now allowed [9–11]. In metals, laser-excited electrons generally transfer their energy to the lattice via electron-phonon coupling, resulting in a kinetic activation of the constituent ions and subsequent lattice melting. As the electron-phonon scattering times are of a few hundred femtoseconds, and more than ten phonon emission events are required per electron for the electron-phonon thermalization, typical ultrashort laser-driven thermal melting occurs in a picosecond timescale [12]. In covalently bonded materials, the formation of strongly laser-driven dense electron-hole plasma leads to the modification of the interatomic potential energy surface (PES) and the ensuing amorphization of crystalline solids while the lattice is still cold, offering an alternative route to phase transition [13–15]. This peculiar phenomenon, called nonthermal melting, has been in the center of heated debates ever since its first experimental observations [16–18]. To understand its underlying mechanism, Stampfli and Bennemann used the tight-binding approach to find out that the transverse acoustic and longitudinal optical phonons become unstable due to dense electron-hole plasma formation [19,20]. This interpretation was later validated by a number of experimental and theoretical studies, and endeavors were made to determine the threshold excitation density for driving nonthermal melting [21–25]. Nonetheless, ultrafast melting at high excitation densities does not seem to involve the nonthermal effect alone. Several studies revealed that the lattice temperature increases to the melting point in ∼100 fs after excitation and the interplay of the thermal and nonthermal effects in subpicosecond lattice melting was also proposed [24,26,27]. These indicate that the determination of thermal and nonthermal melting purely on timescale grounds is irrelevant, and a thorough interrogation of the effect of the modified PES and the kinetic activation of ions is highly desired. Moreover, the exact knowledge of the thermal and nonthermal effects in ultrashort laser-driven materials is very important because the existence of a large heat-affected zone is detrimental to high-precision laser processing, including micromachining and surface treatment [28,29].

Here, we present an approach for quantifying the thermal and nonthermal components involved in the ultrafast Ge disordering through nonadiabatic quantum molecular dynamics (NAQMD) simulations. In this paper, the term "thermal component" refers to the disorder arising from ionic thermal activation regardless of its origin (i.e., excitation of lattice vibration of higher energy), while the "nonthermal component" encompasses disorders other than the thermal disorder. The NAQMD employed in this study describes the electronic excitation within the linear-response time-dependent density functional theory (LR-TDDFT) framework. The electron-ion dynamics are treated nonadiabatically through fewest switches surface hopping (FSSH), in which the energy difference accompanying the interlevel electronic transition is accommodated by ionic velocity adjustment [30–33]. This allows us to concurrently investigate the influence of the modified PES effective in excited electronic states and the nonadiabatic electron-ion interaction on the lattice dynamics.

II. THEORETICAL BACKGROUND

A. Nonadiabatic quantum molecular dynamics

NAQMD adopted in this work [30,31] combines Casida's LR-TDDFT and Tully's FSSH to track the time evolution of

*Corresponding author: yungokihm@postech.ac.kr
†Corresponding author: jhshim@postech.ac.kr

the electronic and ionic states of the femtosecond laser-excited material [32,33]. LR-TDDFT describes the electronic excited states by evaluating their excitation energies in the adiabatic potential surfaces. The ionic forces in electronic excited states may readily be obtained using Hellmann-Feynman theorem. This approach is valid when the electrons stay in adiabatic potential surfaces without moving from one surface to another. Tully's FSSH remedies this limitation by imposing a set of rules for interstate electronic transition and energy conservation, by which the nonadiabatic electron-ion dynamics is described.

In LR-TDDFT adopted in QXMD, electronic excited states are constructed from the ground-state properties obtained by solving the Kohn-Sham (KS) equation [30,31],

$$\hat{H}|\varphi_i\rangle = \left(-\frac{\nabla^2}{2} + \hat{V}_{\text{ext}} + \hat{V}_{\text{H}} + \hat{V}_{\text{xc}}\right)|\varphi_i\rangle = \epsilon_i|\varphi_i\rangle \tag{1}$$

where $\hat{V}_{\text{ext}}$, $\hat{V}_{\text{H}}$, and $\hat{V}_{\text{xc}}$ are the ionic potential, Hartree potential, and exchange correlation (xc) potential; ϵ_i and $|\varphi_i\rangle$ are the ith eigenstate KS energy and orbital, respectively. The KS energies and orbitals are then corrected by including a long-range xc functional to obtain the long-range corrected KS energies, ε_i, and orbitals, $|\psi_i\rangle$. A LR-TDDFT eigenvalue equation is then set up using these long-range corrected KS states and the electronic excitation energies are obtained from the following matrix equation:

$$\begin{pmatrix} A & B \\ B^* & A^* \end{pmatrix}\begin{pmatrix} X_I \\ Y_I \end{pmatrix} = \omega_I \begin{pmatrix} 1 & 0 \\ 0 & -1 \end{pmatrix}\begin{pmatrix} X_I \\ Y_I \end{pmatrix}, \tag{2}$$

where ω_I and $(\boldsymbol{X_I}, \boldsymbol{Y_I})$ are the Ith excited-state excitation energy and the corresponding eigenvector. The matrix elements are the quantities defined by the following ground-state properties:

$$A_{ai\sigma,bj\tau} = \delta_{a,b}\delta_{i,j}\delta_{\sigma,\tau}\,(\varepsilon_{a,\sigma} - \varepsilon_{i,\sigma}) + K_{ai\sigma,bj\tau}, \tag{3}$$

$$B_{ai\sigma,bj\tau} = K_{ai\sigma,bj\tau}, \tag{4}$$

$$\begin{aligned} K_{ai\sigma,bj\tau} =& (\psi^*_{a\sigma}\psi_{i\sigma}|1/r|\psi^*_{j\tau}\psi_{b\tau}) \\ &- \delta_{\sigma,\tau}\left(\psi^*_{a\sigma}\psi_{b\tau}|[\text{erf}(\mu r)]/r|\psi^*_{j\tau}\psi_{i\sigma}\right) \\ &+ \int d\boldsymbol{r}\int d\boldsymbol{r}'\psi^*_{a\sigma}(\boldsymbol{r})\psi_{i\sigma}(\boldsymbol{r})\frac{\delta^2\left(E_{xc} - E_x^{\text{LR}}\right)}{\delta\rho_\sigma(\boldsymbol{r})\delta\rho_\tau(\boldsymbol{r}')} \\ &\times \psi^*_{j\tau}(\boldsymbol{r}')\psi_{b\tau}(\boldsymbol{r}'), \end{aligned} \tag{5}$$

where ρ_σ is the electron density with spin σ and E_{xc} and E_x^{LR} are the xc functional and the long-range part of the Hartree-Fock exchange integral, respectively [31]. The indices $\{i, j\}$ and $\{a, b\}$ are for the occupied and unoccupied KS orbitals, respectively. The many-body wave function of the Ith excited state can be expressed as

$$\begin{aligned} |\Phi_I\rangle &= \sum_{i\in\{\text{occupied}\}}\sum_{a\in\{\text{unoccupied}\}}\sum_{\sigma}\frac{X_{I,ai\sigma} + Y_{I,ai\sigma}}{\sqrt{\omega_I}}\hat{c}^+_{a\sigma}\hat{c}_{i\sigma}|\Phi_0\rangle \\ &= \sum_{ia\sigma} C_{I,ai\sigma}\Phi_{ai\sigma}, \end{aligned} \tag{6}$$

where $|\Phi_0\rangle$ is the Slater determinant of the long-range corrected KS orbitals and $\hat{c}^+_{a\sigma}$ and $\hat{c}^+_{i\sigma}$ are the creation and annihilation operators. The excited-state force acting on the kth nucleus is computed using the Hellmann-Feynman theorem with the non-self-consistency (NSC) correction made for nonzero electronic charge density difference $\delta\rho(\boldsymbol{r}) = \rho_{\text{out}}(\boldsymbol{r}) - \rho_{\text{in}}(\boldsymbol{r})$:

$$\boldsymbol{F}_k = \boldsymbol{F}_k^{\text{Hellmann-Feynman}} + \boldsymbol{F}_k^{\text{NSC}} + \boldsymbol{F}_k^{c}, \tag{7}$$

where $\boldsymbol{F}_k^{\text{Hellmann-Feynman}}, \boldsymbol{F}_k^{\text{NSC}}$, and $\boldsymbol{F}_k^{c}$ are the Hellmann-Feynman force, non-self-consistent force, and nuclear force acting on atom k, respectively.

In FSSH, however, the electrons are described quantum mechanically whereas the ions are treated classically [33]. The electron that initially existed in a single adiabatic potential surface, e.g., the Ith excited state, evolves over time among the excited states obtained through LR-TDDFT with the fixed ionic position

$$|\Psi(\text{t})\rangle = \sum_J C_J(t)|\Phi_J(R(t))\rangle,\ C_J(0) = \delta_{J,I}. \tag{8}$$

The time-evolving expansion coefficients that determine the electronic density at each adiabatic surface at a given time are expressed by the nonadiabatic coupling (NAC) between adiabatic surfaces:

$$\frac{dC_J(t)}{dt} = -\sum_K (i\omega_K\delta_{J,K} + D_{JK})C_K(t), \tag{9}$$

$$D_{JK} = \langle\Phi_J|\frac{\partial}{\partial t}|\Phi_K\rangle = \dot{R}(t)\cdot\langle\Phi_J|\nabla_{\boldsymbol{R}}|\Phi_K\rangle. \tag{10}$$

The NAC element, D_{JK}, gives an overlap integral between the Jth adiabatic surface and the temporal change of the Kth adiabatic surface, providing a nice measure for the electronic transition between the Jth and Kth surfaces. The negative sign on the right-hand side of Eq. (9) indicates that strong nonadiabatic coupling between the Jth and Kth adiabatic surfaces leads to the population leakage of the electrons existing on the Jth adiabatic surface. The time evolution of the expansion coefficients makes it imperative to adjust the electronic population of each adiabatic surface such that they evolve consistently, which is done through electronic hopping between adiabatic surfaces. The hopping rate from the Jth to Kth adiabatic surfaces are governed by their NAC strength,

$$P_{J\to K} = H\left(\frac{2\text{Re}(D_{JK}C_J^*C_K)dt}{C_JC_J^*}\right), \tag{11}$$

where $H(x)$ is the Heaviside step function. The energy difference associated with surface hopping is accommodated by the ionic velocity adjustment in the direction of the NAC vector to meet energy conservation. This also means that when energy change associated with upward transition cannot be compensated by the ionic kinetic energy adjustment, the hopping is frustrated, thereby lowering the upward transition rate compared to the downward transition rate. It was shown that, due to these frustrated hops, FSSH in general satisfies detailed balance with only small deviations in all NAC ranges [34]. The electron-ion energy exchange accompanying electronic adiabatic surface hopping is basically related to the electron-phonon coupling that is often used in the two-temperature

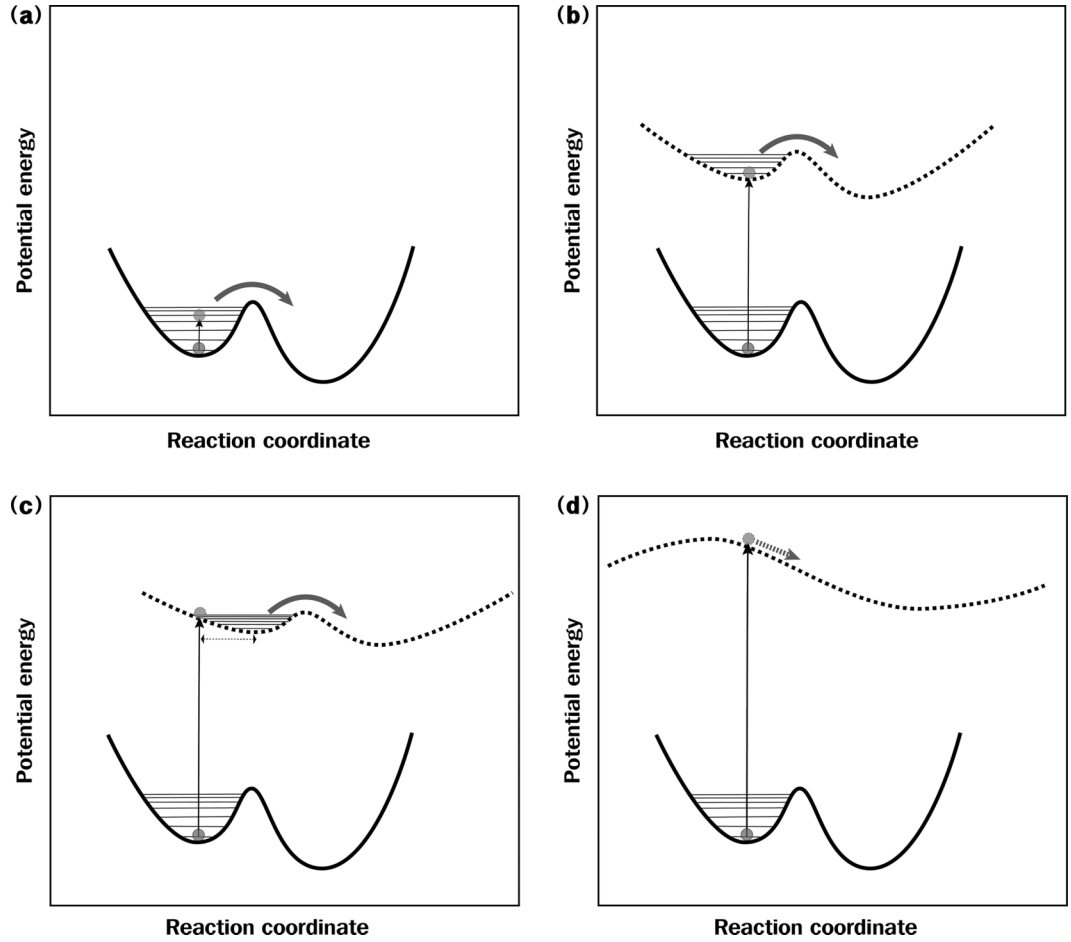

FIG. 1. Schematic representation of fundamental mechanisms involved in ultrashort laser-driven phase transformation of covalently bonded materials. (a) The phase transformation resulting from ionic thermal activation caused by transfer of excited electronic energy to the lattice via electron-phonon coupling. This process is denoted as "th_ep." (b) The phase transformation resulting from weakening of interatomic bonding caused by the PES shape modification. This process is denoted as "bs." (c) The phase transformation resulting from the effects of both the weakened interatomic bonding caused by PES shape modification (bs) and the PES minimum position shift that thermally activates the lattice (th_pes). This process includes overall effects caused by the PES change denoted as "pes." (d) The phase transformation occurring under repulsive PES in high excitation densities. This process includes pes, i.e., both bs and th_pes. The curved solid and dashed lines are the ground- and excited-state PESs, respectively. The gray solid and dashed arrows represent barrier crossing and ionic acceleration, respectively. The dotted arrow indicates the amount of the PES minimum position shift in the reaction coordinate.

model [35,36]

$$\left(\frac{\partial E_e}{\partial t}\right)_{ep} = G(T_l - T_e), \tag{12}$$

where E_e and G are the electron-ion energy exchange and electron-phonon coupling constant, and T_e and T_l are the electronic and ionic temperatures, respectively. Our recent atomistic two-temperature molecular dynamics (TTMD) model incorporates the energy transfer between the electrons and the lattice through ionic velocity rescaling, which is consistent with the FSSH scheme [9]. We applied this TTMD scheme to a number of ultrashort laser-driven nanoparticle systems, successfully interpreting the electronic excitation-driven lattice dynamics in a picosecond timescale [9–11]. Although the NAQMD combining LR-TDDFT and FSSH effectively describes laser-excited electron and ion dynamics, it is limited in describing electron-electron coupling, such as carrier multiplication and Auger recombination [37]. As discussed in Ref. [37], the impact of carrier multiplication can be particularly crucial for inducing a nonthermal effect at high-energy excitation of over five times the band-gap energy. The excitation energy of 1.5 eV used in this work, however, is rather mild, and thus a significant effect of carrier multiplication is unexpected.

B. Description of the fundamental effects

To quantify thermal and nonthermal effects involved in ultrashort laser irradiated Ge, we first define fundamental components associated with PES change and ionic thermal activation. Figure 1 classifies the fundamental mechanisms involved in the femtosecond laser-driven melting transition of covalently bonded materials into three different categories. The process shown in Fig. 1(a) occurs when the excited electrons transition to lower-lying PESs, transferring their energy into lattice thermal energy to conserve the total energy. As, in this process, the ionic thermal activation, i.e.,

the excitation of higher energy lattice vibration, is caused by electron-phonon coupling, we denote this process as "th_ep." Figs. 1(b)–1(d) depict processes resulting from the effects caused by PES change, i.e., effects other than th_ep. Femtosecond laser-driven PES change includes two independent aspects. The first one is modification of the PES shape into a shallower one. Here we only consider the case in which the laser pulse weakens interatomic bonding excluding the opposite case, i.e., bond hardening, as it is less common. The process depicted in Fig. 1(b) entails PES shape modification that is linked to weakening of interatomic bonding and reduction of force constant and potential energy. In this process, the ions are supposed to remain in the lowest vibrational level in the excited electronic PES, and thus the main driver to lattice disordering and phase transition is bond softening and the resultant lowering of the energy barrier. As this effect is exclusively associated with bond softening affecting potential energy, it is nonthermal and is denoted as "bs." The second aspect of the PES change is the shift of the minimum PES position in the reaction coordinate. Its main consequence is instantaneous excitation of the lattice vibration in a new PES, i.e., shifted PES, that is higher in energy than the original one [Fig. 1(c)]. We denote this effect as "th_pes," as it represents ionic thermal activation caused by PES change. Although the origin of this vibrational excitation is nonthermal, i.e., a shift of minimum PES position, this process involves increased thermal energy and lattice temperature, and thus should have direct consequences in lattice disordering. Here we decompose the effect of PES change into PES shape modification and minimum position shift for convenience of understanding. However, these two effects should be concurrent in real systems as depicted in Fig. 1(c), which is denoted as "pes," implying a PES change-driven effect as a whole. Figure 1(d) basically belongs to the category of Fig. 1(c) in which both the PES shape modification (bs) and nonthermally driven ionic thermal activation (th_pes) are present, but in this case the electronic excitation density is strong enough to turn the PES into a repulsive one. In this case, the lattice is expected to make a phase transition within less than a single vibrational period. In the following analyses of the simulation results, the effect originating from bs is categorized as a nonthermal effect whereas the one originating either from th_pes or th_ep is considered a thermal effect. Note that th_pes is included in the thermal effect category, emphasizing the direct role of "effect" rather than "cause" on lattice disordering.

C. Description of constrained simulations and disorder parameter calculation

In this section, we explain our approach for quantifying fundamental components contributing to the total lattice disorder, from which the thermal and nonthermal effects are evaluated. We express the lattice disorder by using a local disorder parameter which is represented by the configurational entropy involving a two-body correlation (S in units of k_B) [38]. The usefulness of this parameter in distinguishing the ordered and disordered phases was well reported in previous studies [10,11,39]. The disorder parameters resulting from the electron-phonon coupling-driven thermal effect (th_ep), PES change-driven thermal effect (th_pes), PES change-driven bond softening effect (bs), and PES change-driven effect (pes) are computed with the lattice structures obtained through constrained simulations. For this, we herein define three independent constrained simulations. First, we define a simulation compatible with the experiment that is conducted in vacuum without energy exchange with the surrounding environment, such as the one of Ref. [40]. NAQMD simulation in microcanonical ensemble (*NVE*) should suffice for reproducing the experimental results if the volume change is negligible. This may be the case with Ge because the atomic volume of Ge at 1100 K, which is a slightly lower temperature than the Ge melting point of 1211 K, is greater than that at 300 K by less than 2% in equilibrium [41]. The situation might not be considerably different in nonequilibrium either. We label this simulation condition with which the total disorder parameter denoted as $S_{\mathrm{tot}}(t)$ is obtained as NVE_NA. Second, we define a simulation in which only the bs effect influences lattice disorder; that is, all thermal effects including th_pes and th_ep are suppressed. This may be accomplished through NAQMD simulation in canonical ensemble (*NVT*), which fixes the lattice volume and temperature to those of the initial condition. We label the simulation condition with which the bs effect-driven lattice disorder parameter, denoted as $S_{\mathrm{bs}}(t)$, is obtained as NVT_NA. Last but not least, a simulation is defined in which only the PES change effect, i.e., pes, is accounted for. In this simulation, bs and th_pes need to be included while suppressing any energy transfer between electronic and lattice systems. This may be accomplished in adiabatic quantum molecular dynamics (AQMD) simulations in which the electron-phonon energy exchange rate expressed as Eq. (13) [35,36] becomes zero:

$$\left(\frac{\partial E_e}{\partial t}\right)_{ep} = \left(\frac{4\pi}{\hbar N_c}\right)\sum_{kk'}\hbar\omega_Q|M_{kk'}|^2 S(k,k')\delta(E_k - E_{k'} + \hbar\omega_Q), \tag{13}$$

where $M_{kk'}$ is the electron-phonon scattering matrix element for the initial and final electronic states with energies E_k and $E_{k'}$. $\hbar\omega_Q$ is the phonon energy and $S(k,k')$ is a thermal factor, respectively. The AQMD simulation in which $M_{kk'} = 0$ for all times is labeled as NVE_AD. The PES change-driven disorder denoted as $S_{\mathrm{pes}}(t)$ is to be obtained through NVE_AD simulations.

The total disorder may be represented as follows with the sum of the disorders originating from bs, th_pes, and th_ep effects:

$$S_{\mathrm{tot}}(t) = S_{\mathrm{bs}}(t) + S_{\mathrm{th\_pes}}(t) + S_{\mathrm{th\_ep}}(t) \ = S_{\mathrm{pes}}(t) + S_{\mathrm{th\_ep}}(t). \tag{14}$$

And the total disorder at t may be obtained from its time derivative:

$$\frac{d}{dt}S_{\mathrm{tot}}(t) = \frac{d}{dt}S_{\mathrm{pes}}(t) \ + \frac{d}{dt}S_{\mathrm{th\_ep}}(t). \tag{15}$$

The disorder parameters are initially identical for all different constrained simulations as they start with the same initial condition and we are interested in obtaining the disorder

increase from the initial value caused by each effect, which allows $S_{\rm bs}(0) = S_{\rm pes}(0) = S_{\rm tot}(0) \equiv S(0)$. Integrating Eq. (15),

$$\begin{aligned} S_{\rm tot}(t) &= S_{\rm tot}(0) + \int_0^t \frac{d}{dt'} S_{\rm tot}(t')dt' \\ &= S(0) + \int_0^t \frac{d}{dt'} S_{\rm pes}(t')dt' + \int_0^t \frac{d}{dt'} S_{\rm th\_ep}(t')dt' \\ &= S_{\rm pes}(t) + \int_0^t \frac{d}{dt'} S_{\rm th\_ep}(t')dt'. \end{aligned} \tag{16}$$

Now, the disorder increase from the initial value caused by electron-phonon coupling is obtained from $S_{\rm tot}(t)$ and $S_{\rm pes}(t)$ as follows:

$$S_{\rm th\_ep}(t) - S_{\rm th\_ep}(0) = S_{\rm tot}(t) - S_{\rm pes}(t). \tag{17}$$

As remarked above, $S_{\rm tot}(t)$ is to be obtained from an NVE_NA simulation. Determination of $S_{\rm pes}(t)$ is more complicated, as it is the portion of total disorder caused by the change of PES in an excited state compared to the ground state. It may be obtained through a hypothetical NVE_AD simulation in which the electron-lattice energy transfer is instantaneously suppressed at each time step in simulation conditions otherwise identical to those of the original NVE_NA. Let the disorder parameter thus obtained be $S_{\rm NVE\_AD}(t)$, then $S_{\rm pes}(t) = S_{\rm NVE\_AD}(t)$. As the electronic occupations for adiabatic states keep changing in NVE_NA, $S_{\rm NVE\_AD}(t)$ cannot be computed in a single simulation. One of the reasonable ways to obtain $S_{\rm NVE\_AD}(t)$ is to compute $dS_{\rm NVE\_AD}(t)/dt$ and then integrate it over time. Assuming that no appreciable change in electronic occupation states would occur in a short time interval, $dS_{\rm NVE\_AD}(t)/dt$ may be approximately obtained from multiple short NVE_AD simulations in which the data produced by an NVE_NA simulation at multiple time points are used as their initial conditions. In other words, in performing a set of NVE_AD simulations for a short time interval Δt, their initial conditions are obtained from longer timescale NVE_NA simulation results at t_k with $t_k = k\Delta t$ and $k = 0, 1, 2, \ldots, N-1$. The initial condition for an NVE_AD simulation requires the knowledge of atomic coordinates and velocities as well as the electronic occupation states at each adiabatic surface. Let $\Omega_{t_k}(t)$ be the disorder parameter obtained from NVE_AD simulation performed for a short time interval Δt using the NVE_NA simulation result at t_k as its initial condition; then the time derivatives $dS_{\rm pes}(t_k)/dt$ and $dS_{\rm NVE\_AD}(t_k)/dt$ at t_k are obtained from its temporal change rate:

$$\frac{d}{dt} S_{\rm pes}(t_k) = \frac{d}{dt} S_{\rm NVE\_AD}(t_k) \approx \frac{\Omega_{t_k}(\Delta t) - \Omega_{t_k}(0)}{\Delta t}. \tag{18}$$

Note that $\Omega_{tk}(0) = S_{\rm NVE\_NA}(t_k)$. The $dS_{\rm NVE\_AD}(t)/dt$ can approximately be found at any t through interpolation of $dS_{\rm NVE\_AD}(t_i)/dt$ and finally $S_{\rm pes}(t)$ and $S_{\rm NVE\_AD}(t)$ are determined for all t from the following relation:

$$S_{\rm pes}(t) = S_{\rm NVE\_AD}(t) = S(0) + \int_0^t \frac{d}{dt'} S_{\rm NVE\_AD}(t')dt'. \tag{19}$$

The PES change-driven thermal effect is obtained from the difference between pes and bs effects:

$$S_{\rm th\_pes}(t) = S_{\rm pes}(t) - S_{\rm bs}(t). \tag{20}$$

III. COMPUTATIONAL DETAILS

In this work, all quantum molecular dynamics (QMD) simulations were performed as implemented in QXMD [30] with a diamond Ge structure in a crystalline density of 5.3234 g cm^{-3}, using a norm-conserving pseudopotential and a periodic boundary condition [42]. The gamma point was used to sample the Brillouin zone. The electronic wave functions were expanded in plane waves with a cutoff energy of 30 Ry. A 3 × 3 × 3 supercell with 216 Ge atoms was first relaxed in their ground state at room temperature for 1 ps through AQMD simulation. A canonical ensemble and an molecular dynamics (MD) time step of 1.2 fs were used. The NAQMD simulation, labeled as NVE_NA in Sec. II C, was performed in microcanonical ensemble for the excited states based on the TDDFT and FSSH methods, with the TDDFT time step of 1 as. The number of electrons corresponding to $n = 3.0\%$, 4.6%, 6.5%, 8.1%, and 10.2% of the valence electrons was initially excited to the empty conduction bands such that the average excitation energy was ∼1.5 eV. The electrons were allowed to transition between the excited states with the atomic velocity rescaled upon transition. The non-self-consistent excited-state forces were computed using a modified Harris-Foulkes approach [31]. Multiple excited AQMD simulations were performed for computing $S_{\rm NVE\_AD}(t)$. As detailed in Sec. II C, the initial conditions for these multiple excited NVE_AD simulations were obtained from a single NVE_NA simulation; that is, the initial atomic coordinates, velocities, and electronic occupation states for each NVE_AD simulation were obtained from the NVE_NA data at $t_k = k\Delta t$ with $\Delta t = 12$ fs and $k = 0, 1, 2, \ldots, N-1$. The interstate electronic transitions were not allowed in NVE_AD simulations. The excited-state NAQMD simulation in canonical ensemble, labeled as NVT_NA in Sec. II C, was performed at room temperature, which suppressed the effects due to the ionic kinetic energy change using a thermostat. All other simulation conditions were identical to those of NVE_NA. The radial distribution function (RDF) and the configurational entropy were obtained from the QMD-simulated atomic coordinates using LAMMPS [38,43].

IV. RESULTS AND DISCUSSION

A. NAQMD simulation in NVE ensemble (NVE_NA)

The excited-state NAQMD simulations were conducted in a microcanonical ensemble with the atomic coordinates and velocities obtained from the equilibration run. Figure 2(a) shows the time evolution of the lattice disorder, which precipitously increased and saturated by 250–410 fs for the high excitation densities ($n \geqslant 6.5\%$). For the low excitation densities, the saturation time was prolonged after the initial quick increase. We define herein the time the disorder parameter saturated and the saturation value as the melting time, t_m, and S_m, respectively (see Fig. S1 in the Supplemental Material [44] and Table I). Once the disorder saturated at $-1.81k_{\rm B}$, the lattice became a diffusive liquid state (Fig. S3 [44]), which

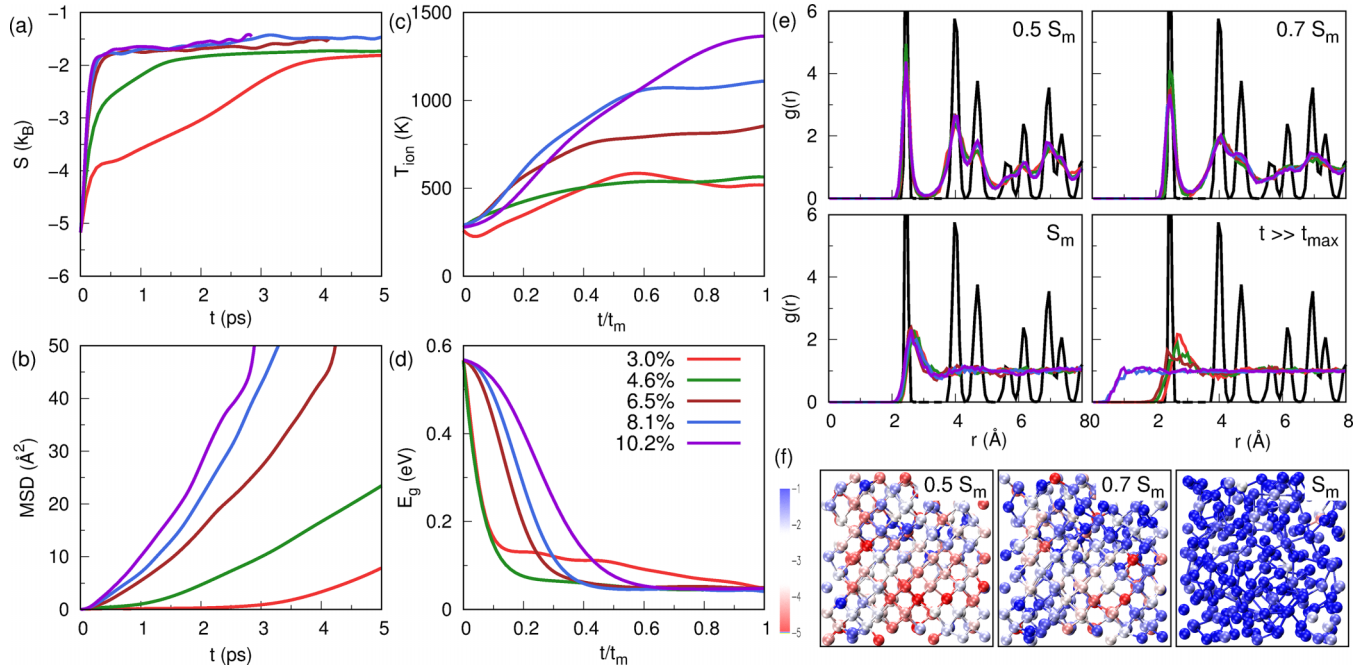

FIG. 2. Results of the excited-state NAQMD simulation in the microcanonical ensemble (NVE_NA). (a) The excitation density-dependent time evolution of the disorder parameter. The time evolution of (b) the MSD, (c) the ionic temperature, and (d) the band-gap energy. (e) The RDFs are denoted for the times the lattice disorder reaches 50% (top left panel), 70% (top right panel), and 100% (bottom left panel) of the maximum disorder and for the time long enough after the maximum disorder is achieved (bottom right panel), and (f) the corresponding lattice structures are shown for $n = 8.1\%$. The atoms are colored according to the disorder parameter.

later became superdiffusive [Fig. 2(b)]. The diffusion coefficients obtained from the linear curve slope after the melting transition ranged from 9.42×10^{-5} to 3.11×10^{-4} cm^2/s and increased with the excitation density increase (Table II). Interestingly, the diffusion coefficients for $n = 4.6\%$ and 3.0% were lower than that of liquid Ge at 1250 K, 1.51×10^{-4} cm^2/s. Figure 2(c) depicts the time evolution of the ionic temperature, which gradually increased until t_m. The ionic temperature at t_m varied depending on the excitation density. That is, the larger the excitation density, the higher the ionic temperature at t_m (Table II). For the highest excitation density ($n = 10.2\%$), the ionic temperature was already 1270 K at t_m, which was above the Ge melting point (1211 K), indicating an intensive thermal energy flow to the lattice. Considering that its t_m of 250 fs was shorter than the room-temperature lattice vibrational period of ~300 fs (Fig. S4 [44]), the PES in this highly excited state presumably turned partially repulsive, resulting in atomic acceleration and subsequent ionic thermal activation and lattice melting as in Fig. 1(d) [21]. In contrast, at the lowest excitation density ($n = 3.0\%$), the lattice temperature at t_m was only 520 K, which was far below the Ge melting point. It is likely that, although it was not repulsive, the interatomic PES was modified in a manner wherein the system overcame the free-energy barrier and transitioned to the liquid phase while the lattice was relatively cold [Fig. 1(b)]. This significant nonthermal effect in ultrafast melting at a low excitation density of 3.0% was quite surprising. The lattice disorder increase resulted in band-gap collapse and phase transformation into a metallic phase [Fig. 2(d)]. The band gap collapsed when the lattice disorder level reached 50–60 % of the saturation value and continued to collapse thereafter. Note that, for $n = 3.0\%$, the band gap persisted longer until it was close to the melting time of 4 ps. The RDFs at different stages of the NAQMD simulation revealed how crystallinity

TABLE I. The melting time (t_m) and its lattice disorder parameter (S_m) for NVE_NA and the time during which maximum lattice disorder is achieved (t_{max}) and its disorder parameter (S_{max}) for NVT_NA.

n (%)	t_m (ps)	S_m (k_B)	t_{max} (ps)	S_{max} (k_B)
10.2	0.25	−1.81	0.52	−2.31
8.1	0.35	−1.81	0.48	−2.60
6.5	0.41	−1.81	0.21	−3.06
4.6	1.6	−1.81	0.20	−3.24
3.0	4.0	−1.81	0.12	−3.90

TABLE II. Ionic temperature and diffusion coefficient at the melting transition obtained under various simulation conditions. NVT_GS indicates ground-state AQMD in an *NVT* ensemble. T_m is the ionic temperature at t_m for NVE_NA and the imposed constant ionic temperature for the other simulation conditions.

Simulation condition	n (%)	T_m (K)	D (10^{-4} cm^2/s)
NVE_NA	10.2	1270	3.11
NVE_NA	8.1	1030	2.55
NVE_NA	6.5	800	1.93
NVE_NA	4.6	600	1.07
NVE_NA	3.0	520	0.94
NVT_NA	14.6	300	0.14
NVT_GS	0	1250	1.51

loss was achieved [Fig. 2(e)]. For all excitation densities, the RDFs started broadening when half of the maximum disorder was achieved (top left panel), implying that the lattice started losing its crystalline order at this stage. As the disordering proceeded further, the RDFs broadened more, and the entire lattice transformed into a liquid state by t_m (bottom left panel). Disordering continued, proceeding further for $n = 10.2\%$ and 8.1%, and the system eventually ended up in an ideal-gas-like phase at a longer timescale, as evidenced by the loss of the first peak at ∼2.5 Å (bottom right panel). When a liquid evaporates into a gas, the system volume undergoes a significant increase. Consequently, the *NVT* and *NVE* simulations may not be suitable for this regime. The atomic structures obtained from the NAQMD simulation demonstrated that melting seeds formed inside the laser-excited Ge lattice and propagated over time to the entire lattice [Fig. 2(f)].

B. Comparison of NAQMD simulation and experimental results

To validate the quality of our NAQMD simulation results, we compared the excitation density dependence of melting time obtained with NVE_NA simulations and those determined elsewhere using time-resolved x-ray diffraction and resonant x-ray scattering [40]. However, whereas our melting time data were obtained with NAQMD as a function of excitation density, n, those of the experiment were determined as a function of absorbed laser fluence, F. For consistency, we first made a conversion of n to F. For this, we assumed that the number of excited electrons per unit volume, N, linearly increased at low fluences but saturated at large fluences as follows:

$$N = N_\infty(1 - e^{-F/\xi}), \tag{21}$$

where N and N_∞ are the volume density of the excited electrons at a given fluence and at infinite fluence, respectively; F and ξ are the absorbed laser fluence and a constant, respectively. We used as N_∞ the valence electron density of $176.6 \times 10^{21}\text{cm}^{-3}$. ξ was determined from the fact that N linearly increased with F at low fluences following Supplemental Material S7 of Lee *et al.* which gave a ξ of 2440 mJ/cm^2 [40]. Figure 3(a) shows the comparison of the melting time obtained with NAQMD and experiment. One can see that NAQMD gives melting times reasonably consistent with those of experiment, indicating that our NAQMD simulation reasonably reproduced experimental data.

To further assess the quality of our NAQMD simulation results, we compared the trend of the mean square displacement (MSD) data obtained from our NVE_NA simulations with that of Si reported in Ref. [45]. Zijlstra *et al.* performed *ab initio* molecular dynamics simulations to investigate the atomic motion of the femtosecond laser-irradiated Si. At strongly driven conditions of $n \geqslant 9.3\%$, they found out that Si atoms that initially were bound in harmonic PESs started accelerating on a repulsive PES after ∼100 fs, subsequently undergoing superdiffusive motion and then transitioning to fractionally diffusive followed by normally diffusive atomic motions [Fig. 3(b)]. According to our MSD data, at $n = 14.6\%$ and 20.0%, Ge atoms directly transitioned from harmonic to normally diffusive motion at around 100–200 fs [Fig. 3(c)]. We could not find any clear indication

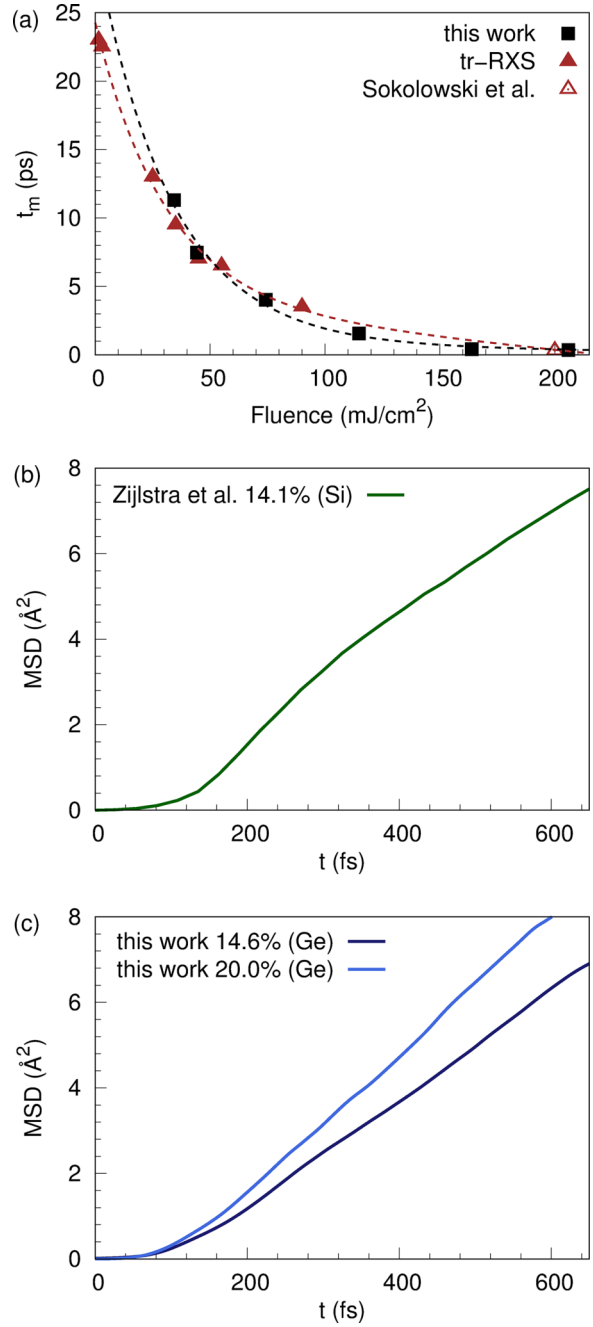

FIG. 3. Comparison of the NVE_NA simulation and experimental results. (a) The fluence dependence of melting time of Ge, where the conversion of the excitation density to the absorbed fluence was made using the nonlinear model in Eq. (21). Our simulation results compare well with those of the time-resolved resonant x-ray scattering experiment [40] and Sokolowski *et al.* [23]. (b) Subpicosecond MSD data of Si reported by Zijlstra *et al.* [45]. (c) Subpicosecond MSD data of Ge obtained with NVE_NA simulations for comparison with (b).

for intermediate states related to superdiffusive or fractionally diffusive atomic motions. These discrepancies may stem from the fact that the Ge atomic weight is 2.5 times larger than that of Si, but we see that the overall trend of our data for Ge reasonably agrees with that of Si reported by Zijlstra *et al.* [45].

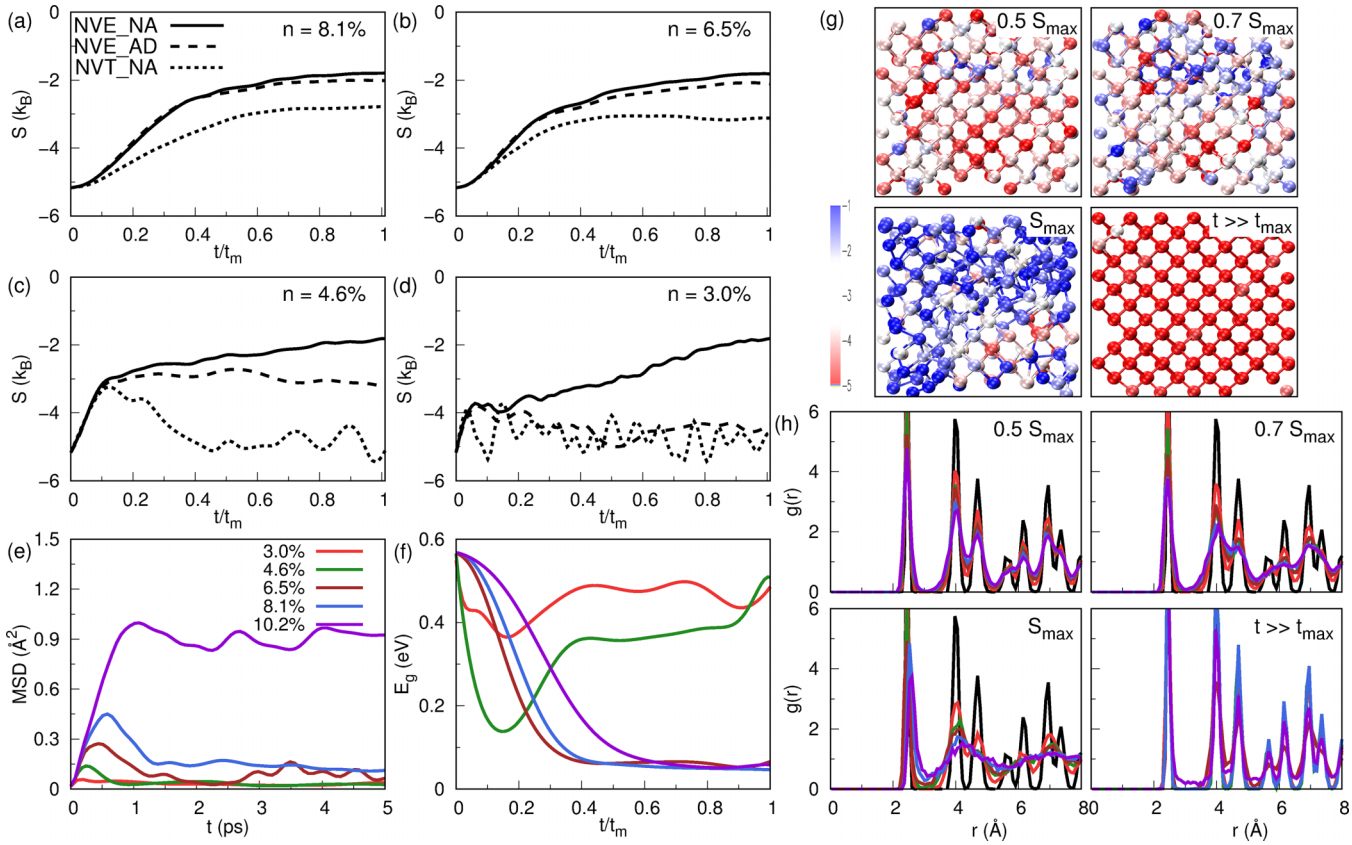

FIG. 4. Results of the various excited-state QMD simulations. A comparison of the disorder parameter time evolution among [(a)–(d)] NVE_NA, NVE_AD, and NVT_NA, and [(e)–(h)] the NVT_NA results. The excitation density-dependent time evolution of (e) MSD and (f) band-gap energy. (g) The lattice structures and (h) the RDFs are shown for the times during which the lattice disorder reaches 50% (top left panel), 70% (top right panel), and 100% (bottom left panel) of the maximum disorder achieved by NVT_NA and for the time long enough after the maximum disorder by NVT_NA was achieved (bottom right panel).

C. AQMD simulation in NVE ensemble (NVE_AD)

We performed additional QMD simulations to dissect the components involved in ultrafast processes. First, we introduced excited-state AQMD simulations as described in Sec. II C (i.e., NVE_AD). Our goal with the NVE_AD simulations was to selectively obtain the disorder parameter of NVE_NA at a given time t caused by PES change. Unlike NVE_NA, these simulations disallowed the electronic transition between excited states. As a result, energy transfer from the excited electrons to ions via electron-phonon coupling that leads to the ionic thermal activation shown in Fig. 1(a) was blocked. However, the excited electronic states may modify the interatomic PES in a way to reduce the energy barrier as shown in Figs. 1(b) and 1(c) and, at high enough excitation densities, turn the PES into a repulsive one that increases the ionic temperature via atomic acceleration [Fig. 1(d)]. These effects were to be dealt with in NVE_AD simulations. The impediment to obtaining the PES change-driven disorder parameter, $S_{\rm pes}(t)$, from a single NVE_AD simulation was that the time-dependent band occupation states of NVE_NA at a given time instance t could not be incorporated correctly in NVE_AD as the electrons kept remaining at the initial excited states. To ensure that the NVE_AD simulations were performed such that the time-dependent electronic band occupation states of NVE_NA were correctly reflected in obtaining $S_{\rm pes}(t)$, we performed multiple NVE_AD simulations for a short time interval of $\Delta t = 12$ fs as described in Sec. II C. We assumed that no appreciable change in the electronic occupation states would occur for 12 fs, a short enough time compared to the Ge electron-phonon scattering time of 1.2 ps [46]. From these short NVE_AD simulations, $dS_{\rm NVE\_AD}(t_i)/dt$ was obtained first and, with interpolation and subsequent integration, $S_{\rm NVE\_AD}(t)$ was obtained [Figs. 4(a)–4(d)].

D. NAQMD simulation in *NVT* ensemble (NVT_NA)

We also performed NAQMD simulations starting with the initial conditions identical to those of the original NVE_NA runs but in this case in a canonical (*NVT*) ensemble at 300 K (i.e., NVT_NA). In this simulation condition, the ionic thermal activation beyond 300 K was suppressed by a thermostat; thus, only the effects originating from the Ge-Ge bond softening caused by the electron-hole plasma formation were considered. In this manner, we can segregate the fundamental mechanisms driving the ultrafast phase transformation into the components of the thermal and nonthermal disorders.

E. Comparison of various QMD simulation results

Figures 4(a)–4(d) compare the time evolutions of the disorder parameter of up to t_m for $n = 8.1\%$, 6.5%, 4.6%, and

3.0%, respectively. For $n = 8.1\%$, the disorder obtained with NVE_AD (dashed line) was comparable to that of NVE_NA (solid line), indicating the driven disorder was dominated by the PES change and the contribution of the ionic thermal activation arising from the electron-phonon coupling was comparatively negligible. The NVE_AD disorder became smaller than that of NVE_NA as the excitation density decreased, implying that the ionic thermal activation caused by the electron-phonon coupling started to play its role. Conversely, NVT_NA (dotted line) provided a much different disorder evolution. The disorder parameter initially underwent an upsurge for hundreds of femtoseconds, as in NVE_NA (or NVE_AD). A downturn then followed instead of a saturation [Figs. 4(c) and 4(d)]. The time the initial upsurge of the disorder parameter is completed in NVT_NA and its value are denoted as $t_{\max}$ and $S_{\max}$, respectively (Fig. S2 [44], Table I). The nonlinearity of the MSD curves of NVT_NA revealed that the phase transformed by bond softening was far from the liquid state. Instead of continuing to increase, the MSD either decreased again ($n \leqslant 8.1\%$) or remained constant ($n = 10.2\%$) until 5 ps. Bond softening alone was insufficient in driving the disorder up to the level achieved by typical laser excitation. In line with the disorder trend, the band-gap energy profiles of NVT_NA were also quite different from those of NVE_NA. The band-gap energy briefly decreased, and then started to increase again at ~1 ps, eventually recovering the original level in a longer timescale. The lattice structure and the RDFs in Figs. 4(g) and 4(h) revealed that the lattice did not completely lose but retained some order at $t_{\max}$ and regained a complete order at a longer timescale. We ran an NVT_NA simulation for $n = 14.6\%$ to determine if this was the case for an even higher excitation density regime (Fig. S5 [44]). The disorder parameter of NVT_NA saturated, but at a $0.5k_B$ value less than that of NVE_NA. The MSD became slightly linear, but the diffusivity was an order of magnitude smaller than that of liquid Ge at 1250 K. In other words, without ionic thermal activation, the normal liquidlike state is hardly achievable with the bond softening effect alone.

F. Quantification of the ultrashort laser-driven disorder components

We quantified the thermal and nonthermal contributions to the ultrafast process of laser-excited Ge by dissecting the total disorder obtained by the above-mentioned simulations. The total disorder obtained by NVE_NA corresponded to the experimentally measured value and encompassed the nonthermal and thermal components. The PES change-driven disorder was obtained from NVE_AD. The nonthermal component involving only the bond softening effect was obtained from NVT_NA. The thermal component in turn comprised the ionic thermal activation driven by the PES change and electron-phonon coupling. The former may be determined from the difference between the NVE_AD and NVT_NA disorders, whereas the latter may be figured out from that between NVE_NA and NVE_AD. They are described at each time instance as follows:

$$\mu_{\text{tot}}(t) = S_{\text{NVE\_NA}}(t) - S_{300\text{K}}(t), \tag{22}$$

$$\mu_{\text{pes}}(t) = \begin{cases} S_{\text{NVE\_AD}}(t) - S_{300\text{K}}(t) & \left(t \leqslant t_{\max}^{\text{AD}}\right) \\ S_{\text{NVE\_AD}}\left(t_{\max}^{\text{AD}}\right) - S_{300\text{K}}\left(t_{\max}^{\text{AD}}\right) & \left(t > t_{\max}^{\text{AD}}\right), \end{cases} \tag{23}$$

$$\mu_{\text{bs}}(t) = \begin{cases} S_{\text{NVT\_NA}}(t) - S_{300\text{K}}(t) & (t \leqslant t_{\max}) \\ S_{\text{NVT\_NA}}(t_{\max}) - S_{300\text{K}}(t_{\max}) & (t > t_{\max}), \end{cases} \tag{24}$$

$$\mu_{\text{th\_pes}}(t) = \mu_{\text{pes}}(t) - \mu_{\text{bs}}(t), \tag{25}$$

$$\mu_{\text{th\_ep}}(t) = \mu_{\text{tot}}(t) - \mu_{\text{pes}}(t), \tag{26}$$

where $S_{\text{NVE\_NA}}$, $S_{\text{NVE\_AD}}$, and $S_{\text{NVT\_NA}}$ are the disorder parameters obtained from NVE_NA, NVT_NA, and NVE_AD simulations, respectively; $t_{\max}$ and $t_{\max}^{\text{AD}}$ are the times during which the maximum disorder was achieved in NVT_NA and NVE_AD, respectively; $\mu_{\text{tot}}(t)$, $\mu_{\text{pes}}(t)$, and $\mu_{\text{bs}}(t)$ are the total disorder, PES change-driven disorder, and bond-softening-driven nonthermal disorder relative to the room-temperature values, and $\mu_{\text{th\_pes}}(t)$, $\mu_{\text{th\_ep}}(t)$ are the thermal disorders associated with the ionic kinetic activation caused by the PES change and electron-phonon coupling, respectively. $\mu_{\text{pes}}(t)$ and $\mu_{\text{bs}}(t)$ are driven by the PES change caused by the electronic excitation, and thus increase with increased carrier density and decay with the carrier relaxation. However, the driven disorders by the PES change and electron-phonon coupling contribute cooperatively to $\mu_{\text{tot}}(t)$, which keeps increasing over time. Therefore, we assumed that once the contributions of $\mu_{\text{bs}}(t_{\max})$ and $\mu_{\text{pes}}(t_{\max}^{\text{AD}})$ were added to the total disorder, they remained henceforward. The fractions of the nonthermal and thermal contributions to the total disorder are written as follows:

$$f_{\text{nth}}(t) = \frac{\mu_{\text{bs}}(t)}{\mu_{\text{tot}}(t)}, \tag{27}$$

$$f_{\text{th}}(t) = \frac{\mu_{\text{th\_pes}}(t) + \mu_{\text{th\_ep}}(t)}{\mu_{\text{tot}}(t)}. \tag{28}$$

Figure 5 shows the time-dependent contribution of various disorder components to the total disorder of up to t_m. At the early disordering stage, bond softening was dominant for all excitation densities, and the thermal disorder caused by the electron-phonon coupling was relatively insignificant [Figs. 5(a) and 5(c)]. The PES change-driven thermal disorder tended to increase over time but basically did not contribute for $n = 3.0\%$ until melting occurred [Fig. 5(b)]. In short, the PES became far from repulsive at this low excitation level. Figure 5(d) illustrates the time evolution of the percent nonthermal contribution to the total disorder. For all excitation densities, the nonthermal effect dominated in the beginning, but decreased over time until melting occurred. As expected, the percent nonthermal contribution at t_m became larger with the increasing excitation density [Fig. 5(e)]. Interestingly, even at the highest excitation density ($n = 10.2\%$), the phase transition did not occur via the nonthermal effect alone; that is, 28% of the disorder originated from the thermal component. The total thermal effect of 28% in a short melting time of 250 fs should be related to the high lattice temperature of 1270 K at t_m, which indicates the PES presumably turned strongly repulsive, resulting in ionic kinetic activation. Without bond softening, however, the lattice would have been in a superheated state. Likewise, the phase transition at the lowest excitation density ($n = 3.0\%$) that occurred in 4 ps

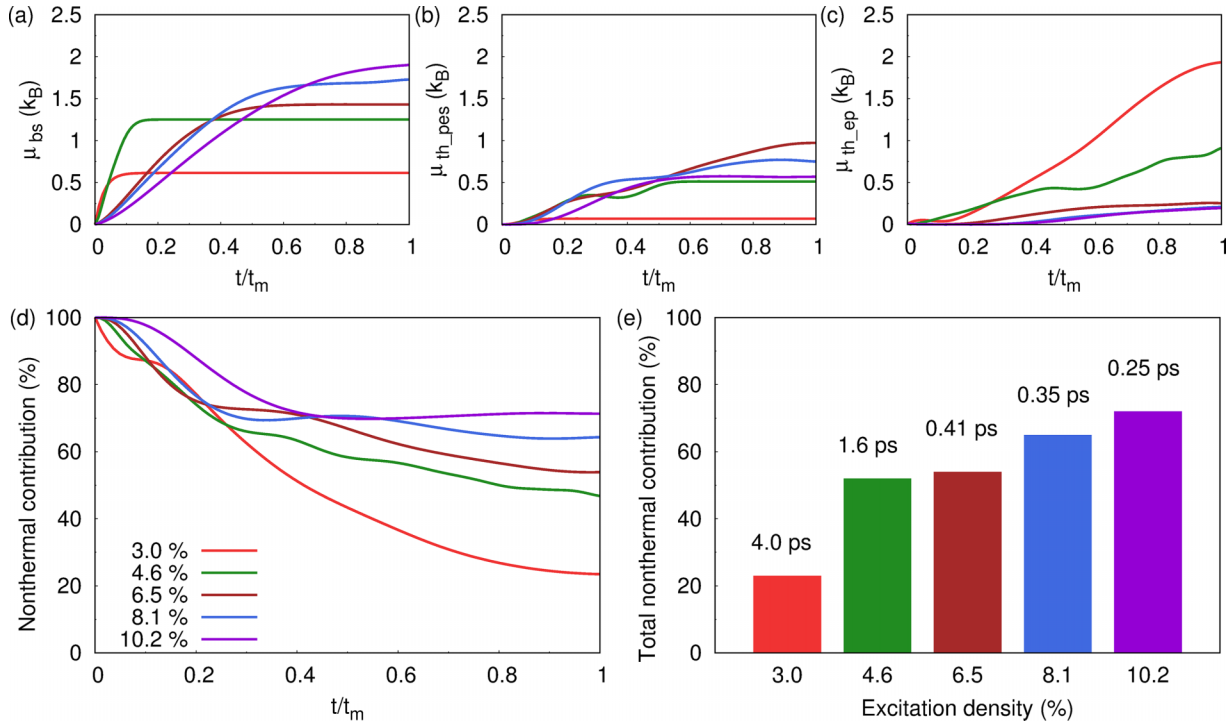

FIG. 5. Time-dependent contribution of various disorder components to the total disorder. (a) Nonthermal disorder component originating from the covalent bond softening. Thermal disorder component associated with (b) the PES change and (c) electron-phonon coupling. (d) Time evolution of the nonthermal contribution to the total disorder. (e) Bar graph of the nonthermal contribution to the total disorder at the melting time, with the number on top of each bar indicating the melting time.

involved approximately 23% of the nonthermal component. Although it is contradictory to the previous notion that the picosecond timescale melting is thermal, considering the low lattice temperature of 520 K at t_m, such a decent amount of nonthermal effect involved in the picosecond melting transition seems reasonable. These results together suggest that the ultrashort laser-driven phase transition involves both thermal and nonthermal elements. Their contribution to the system's net disorder is determined by the electronic excitation density.

V. SUMMARY

In conclusion, we performed herein a nonadiabatic quantum molecular dynamics simulation under the following disparate conditions to understand the underlying mechanism of the femtosecond laser-driven melting of Ge: without constraints (NVE_NA), without interlevel electronic transitions (NVE_AD), and with interlevel electronic transitions but keeping the ionic temperature at room temperature (NVT_NA). These simulation conditions allowed us to investigate the underlying mechanism of the ultrafast phase transformation by segregating the thermal and nonthermal effects into fundamental constituent elements. Our results showed that the nonthermal (bond softening) effect dominated the early disordering stage. However, the eventual thermal or nonthermal contribution to the total disorder depended on the electronic excitation density, with the increased nonthermal effects for the higher excitation densities. The nonthermal contributions during the phase transition were 72% and 23% for the highest and lowest excitation densities, respectively. These corresponded to the excitation densities of $n = 10.2\%$ and 3.0%, which respectively gave melting times of 250 fs and 4 ps. Therefore, we conclude that, irrespective of the excitation density, the femtosecond laser-driven phase transition involves both thermal and nonthermal elements in it, but with the level of their effects being regulated by the electronic excitation density. Our result not only provides an understanding of the fundamental mechanisms of the ultrashort laser-driven phase transition, but also opens up an avenue for using optimal laser parameters in material processing.

ACKNOWLEDGMENTS

We thank Fuyuki Shimojo for kindly helping us in using QXMD. This work was supported by the National Research Foundation of Korea (Grants No. 2018R1D1A1B07040727, No. 2020R1A5A1019141, No. 2021R1A2C1006329, and No. 2021R1A2C2010972) and the National Supercomputing Center of Korea.

[1] G. Sciaini, M. Harb, S. G. Kruglik, T. Payer, C. T. Hebeisen, F. J. M. Z. Heringdorf, M. Yamaguchi, M. H. V. Hoegen, R. Ernstorfer, and R. J. D. Miller, Electronic acceleration of atomic motions and disordering in bismuth, Nature (London) **458**, 56 (2009).

[2] A. M. Lindenberg, J. Larsson, K. Sokolowski-Tinten, K. J. Gaffney, C. Blome, O. Synnergren, J. Sheppard, C. Caleman, A. G. MacPhee, D. Weinstein *et al.*, Atomic-scale visualization of inertial dynamics, Science **308**, 392 (2005).

[3] R. Ernstorfer, M. Harb, C. T. Hebeisen, G. Sciaini, T. Dartigalongue, and R. J. D. Miller, The formation of warm dense matter: Experimental evidence for electronic bond hardening in gold, Science **323**, 1033 (2009).

[4] K. Sokolowski-Tinten, C. Blome, J. Blums, A. Cavalleri, C. Dietrich, A. Tarasevitch, I. Uschmann, E. Forster, M. Kammler, M. Horn-von-Hoegen *et al.*, Femtosecond x-ray measurement of coherent lattice vibrations near the Lindemann stability limit, Nature (London) **422**, 287 (2003).

[5] V. Recoules, J. Clérouin, G. Zérah, P. M. Anglade, and S. Mazevet, Effect of intense laser irradiation on the lattice stability of semiconductors and metals, Phys. Rev. Lett. **96**, 055503 (2006).

[6] V. R. Morrison, R. P. Chatelain, K. L. Tiwari, A. Hendaoui, A. Bruhacs, M. Chaker, and B. J. Siwick, A photoinduced metal-like phase of monoclinic VO_2 revealed by ultrafast electron diffraction, Science **346**, 445 (2014).

[7] D. Wegkamp, M. Herzog, L. Xian, M. Gatti, P. Cudazzo, C. L. McGahan, R. E. Marvel, R. F. Haglund, Jr., A. Rubio, M. Wolf *et al.*, Instantaneous band gap collapse in photoexcited monoclinic VO_2 due to photocarrier doping, Phys. Rev. Lett. **113**, 216401 (2014).

[8] M. Z. Mo, Z. Chen, R. K. Li, M. Dunning, B. B. L. Witte, J. K. Baldwin, L. B. Fletcher, J. B. Kim, A. Ng, R. Redmer *et al.*, Heterogeneous to homogeneous melting transition visualized with ultrafast electron diffraction, Science **360**, 1451 (2018).

[9] Y. Ihm, D. H. Cho, D. Sung, D. Nam, C. Jung, T. Sato, S. Kim, J. Park, S. Kim, M. Gallagher-Jones *et al.*, Direct observation of picosecond melting and disintegration of metallic nanoparticles, Nat. Commun. **10**, 2411 (2019).

[10] C. Jung, Y. Ihm, D. Cho, H. Lee, D. Nam, S. Kim, I. T. Eom, J. Park, C. Kim, Y. Kim *et al.*, Inducing thermodynamically blocked atomic ordering via strongly driven nonequilibrium kinetics, Sci. Adv. **7**, eabj8552 (2021).

[11] J. Shin, C. Jung, Y. Ihm, S. P. Heo, D. Nam, S. Kim, M. Kim, I. Eom, J. H. Shim, D. Noh *et al.*, Ultrafast energy transfer process in confined gold nanospheres revealed by femtosecond x-ray imaging and diffraction, Nano Lett. **23**, 1481 (2023).

[12] Y. Siegal, E. N. Glezer, L. Huang, and E. Mazur, Laser-induced phase-transitions in semiconductors, Annu. Rev. Mater. Sci. **25**, 223 (1995).

[13] B. Rethfeld, D. S. Ivanov, M. E. Garcia, and S. I. Anisimov, Modelling ultrafast laser ablation, J. Phys. D: Appl. Phys. **50**, 193001 (2017).

[14] A. Rousse, C. Rischel, S. Fourmaux, I. Uschmann, S. Sebban, G. Grillon, P. Balcou, E. Foster, J. P. Geindre, P. Audebert *et al.*, Non-thermal melting in semiconductors measured at femtosecond resolution, Nature (London) **410**, 65 (2001).

[15] C. W. Siders, A. Cavalleri, K. Sokolowski-Tinten, C. Toth, T. Guo, M. Kammler, M. H. von Hoegen, K. R. Wilson, D. von der Linde, and C. P. J. Barty, Detection of nonthermal melting by ultrafast x-ray diffraction, Science **286**, 1340 (1999).

[16] C. V. Shank, R. Yen, and C. Hirlimann, Femtosecond-time-resolved surface structural dynamics of optically excited silicon, Phys. Rev. Lett. **51**, 900 (1983).

[17] H. W. K. Tom, G. D. Aumiller, and C. H. Britocruz, Time-resolved study of laser-induced disorder of Si surfaces, Phys. Rev. Lett. **60**, 1438 (1988).

[18] J. A. Van Vechten, R. Tsu, and F. W. Saris, Nonthermal pulsed laser annealing of Si; plasma annealing, Phys. Lett. A **74**, 422 (1979).

[19] P. Stampfli and K. H. Bennemann, Theory for the instability of the diamond structure of Si, Ge, and C induced by a dense electron-hole plasma, Phys. Rev. B **42**, 7163 (1990).

[20] P. Stampfli and K. H. Bennemann, Dynamical theory of the laser-induced lattice instability of silicon, Phys. Rev. B **46**, 10686 (1992).

[21] E. S. Zijlstra, J. Walkenhorst, and M. E. Garcia, Anharmonic noninertial lattice dynamics during ultrafast nonthermal melting of InSb, Phys. Rev. Lett. **101**, 135701 (2008).

[22] T. Zier, E. S. Zijlstra, A. Kalitsov, I. Theodonis, and M. E. Garcia, Signatures of nonthermal melting, Struct. Dyn. **2**, 54101 (2015).

[23] K. Sokolowski-Tinten, C. Blome, C. Dietrich, A. Tarasevitch, M. H. von Hoegen, D. von der Linde, A. Cavalleri, J. Squier, and M. Kammler, Femtosecond x-ray measurement of ultrafast melting and large acoustic transients, Phys. Rev. Lett. **87**, 225701 (2001).

[24] P. L. Silvestrelli, A. Alavi, M. Parrinello, and D. Frenkel, *Ab initio* molecular dynamics simulation of laser melting of silicon, Phys. Rev. Lett. **77**, 3149 (1996).

[25] D. M. Fritz *et al.*, Ultrafast bond softening in bismuth: Mapping a solid's interatomic potential with x-rays, Science **315**, 633 (2007).

[26] N. Medvedev, Z. Li, and B. Ziaja, Thermal and nonthermal melting of silicon under femtosecond x-ray irradiation, Phys. Rev. B **91**, 054113 (2015).

[27] N. Medvedev and A. E. Volkov, Nonthermal acceleration of atoms as a mechanism of fast lattice heating in ion tracks, J. Appl. Phys. **131**, 225903 (2022).

[28] K. C. Phillips, H. H. Gandhi, E. Mazur, and S. K. Sundaram, Ultrafast laser processing of materials: a review, Adv. Opt. Photonics **7**, 684 (2015).

[29] M. J. Abere, M. L. Zhong, J. Kruger, and J. Bonse, Ultrafast laser-induced morphological transformations, MRS Bull. **41**, 969 (2016).

[30] F. Shimojo, S. Fukushima, H. Kumazoe, M. Misawa, S. Ohmura, P. Rajak, K. Shimamura, L. B. Oftelie, S. Tiwari, R. K. Kalia *et al.*, QXMD: An open-source program for nonadiabatic quantum molecular dynamics, Softwarex **10**, 100307 (2019).

[31] F. Shimojo, S. Ohmura, W. W. Mou, R. K. Kalia, A. Nakano, and P. Vashishta, Large nonadiabatic quantum molecular dynamics simulations on parallel computers, Comput. Phys. Commun. **184**, 1 (2013).

[32] M. E. Casida and M. Huix-Rotllant, Progress in time-dependent density-functional theory, Annu. Rev. Phys. Chem. **63**, 287 (2012).

[33] J. C. Tully, Molecular-dynamics with electronic-transitions, J. Chem. Phys. **93**, 1061 (1990).

[34] J. R. Schmidt, P. V. Parandekar, and J. C. Tully, Mixed quantum-classical equilibrium: Surface hopping, J. Chem. Phys. **129** 044104 (2008).

[35] P. B. Allen, Theory of thermal relaxation of electrons in metals, Phys. Rev. Lett. **59**, 1460 (1987).

[36] Z. Lin, L. V. Zhigilei, and V. Celli, Electron-phonon coupling and electron heat capacity of metals under conditions of strong electron-phonon nonequilibrium, Phys. Rev. B **77**, 075133 (2008).

[37] J. Bang, Y. Y. Sun, X.-Q. Liu, F. Gao, and S. B. Zhang, Carrier-multiplication-induced structural change during ultrafast carrier relaxation and nonthermal phase transition in semiconductors, Phys. Rev. Lett. **117** 126402 (2016).

[38] P. M. Piaggi and M. Parrinello, Entropy based fingerprint for local crystalline order, J. Chem. Phys. **147**, 114112 (2017).

[39] H. Y. Niu, P. M. Piaggi, M. Invernizzi, and M. Parrinello, Molecular dynamics simulations of liquid silica crystallization, Proc. Natl. Acad. Sci. USA **115**, 5348 (2018).

[40] H. Lee, J. Y. Ahn, S. H. Chun, D. H. Cho, D. Sung, C. Jung, J. Shin, J. Hwang, S. S. Ha, H. Jang *et al.*, Observing femtosecond orbital dynamics in ultrafast Ge melting with time-resolved resonant x-ray scattering, IUCrJ **10**, 700 (2023).

[41] E.-H. Kim, Y. H. Shin, and B.-J. Lee, A modified embedded-atom method interatomic potential for germanium, Calphad: Comput. Coupling Phase Diagrams Thermochem. **32**, 34 (2008).

[42] L. Kleinman and D. M. Bylander, Efficacious form for model pseudopotentials, Phys. Rev. Lett. **48**, 1425 (1982).

[43] S. Plimpton, Fast parallel algorithms for short-range molecular-dynamics, J. Comput. Phys. **117**, 1 (1995).

[44] See Supplemental Material at http://link.aps.org/supplemental/10.1103/PhysRevB.109.174306 for the determination of t_m and S_m, $t_{\max}$ and $S_{\max}$; MSD curves right after t_m; oscillatory disorder parameter at room temperature; and NVT_NA simulation results at $n = 14.6\%$.

[45] E. S. Zijlstra, A. Kalitsov, T. Zier, and M. E. Garcia, Fractional diffusion in silicon, Adv. Mater. **25**, 5605 (2013).

[46] K. Tanaka, H. Ohtake, and T. Suemoto, Determination of intervalley scattering time in germanium by subpicosecond time-resolved Raman spectroscopy, Phys. Rev. Lett. **71**, 1935 (1993).